

***Ab initio* electronic structure of metallized NiS₂ in the noncollinear magnetic phase**Pascal Reiss ^{1,2,3,*}, Sven Friedemann ⁴, and F. Malte Grosche ²¹*Max-Planck Institute for Solid State Research, 70569 Stuttgart, Germany*²*Cavendish Laboratory, University of Cambridge, Cambridge CB3 0HE, United Kingdom*³*Clarendon Laboratory, Department of Physics, University of Oxford, Oxford OX1 3PU, United Kingdom*⁴*H. H. Wills Laboratory, University of Bristol, Bristol BS8 1TL, United Kingdom*

(Received 2 August 2022; revised 21 October 2022; accepted 24 October 2022; published 18 November 2022)

We investigate the electronic structure of the archetypical Mott insulator NiS₂ by means of density functional theory calculations in which we explicitly account for the noncollinear antiferromagnetic order, as recently established in the isoelectronic analog Ni(S, Se)₂. For metallic NiS₂ under high pressures, our calculations predict a Fermi surface topology and volume which are in excellent agreement with recent quantum oscillation studies. However, we find that density functional theory wrongly predicts a metallic ground state even at ambient pressures, similar to previous nonmagnetic or collinear antiferromagnetic models. By including a Hubbard interaction U and an on-site exchange interaction J , the metallic phase is suppressed, but even such an extended model fails to describe the nature of the metal-to-insulating phase transition and describes the insulating phase itself incorrectly. These results highlight the importance of more sophisticated computational approaches even deep in the insulating phase, far away from the Mott insulating phase transition.

DOI: [10.1103/PhysRevB.106.205131](https://doi.org/10.1103/PhysRevB.106.205131)**I. INTRODUCTION**

One of the most fundamental characteristics of quantum materials is whether their ground state is metallic or electrically insulating. In the standard theory of condensed matter, Landau's Fermi liquid theory, metals have a Fermi surface whereas insulators do not. By Fermi surface we understand a surface in momentum space on which charged, fermionic low-energy excitations are possible, known as Landau's quasiparticles. They resemble the band electrons from which they arise, but they may acquire renormalized parameters, such as an effective mass. In the electronic spectral function, they are reflected as a coherent resonance peak of weight $z < 1$, contrasting with the remaining seemingly incoherent background contributions.

The profound difference between the presence or lack of a Fermi surface allows for two distinct possibilities for how electronic conduction is lost across continuous metal-to-insulator transitions [1]. Either the Fermi surface shrinks and disappears, which corresponds to a reduction of charge carrier numbers, or the charge carriers slow down and eventually localize, which corresponds to the quasiparticle weight z going to zero and thereby to a loss of electronic coherence at the Fermi energy. Distinguishing between these two

pictures is particularly important for the metal-to-Mott-insulator transition. For Mott insulators, band theory including density functional theory (DFT) within standard approximations such as the local density approximation (LDA) predicts a metallic ground state in contrast to the experimental observation of a vanishing electrical conductivity at low temperatures [2]. Therefore, to account for Mott insulating phases, it is necessary to consider the effects of strong electronic correlations. Dynamical mean-field theory (DMFT) calculations and the seminal work by Brinkman and Rice predict a diverging quasiparticle mass at the Fermi level before the gap opens at the brink of the insulating phase [3,4]. At the same time, understanding the transition between a correlated metal and a Mott insulator not only is of fundamental interest but also has profound implications for the cuprate [5] and organic charge-transfer superconductors [6] where Mott insulating phases have been identified. Moreover, orbital-dependent Mott physics has also been discussed for the iron-pnictide superconductors [7].

Experimentally, a metallic phase can be recovered usually by means of hydrostatic or chemical pressure [8–11]. However, following the evolution of electronic correlations across the metal-to-Mott-insulator transition has proved challenging. Taking the archetypical Mott insulator NiS₂ as an example, electronic transport [12–14], thermodynamic [15,16], optical [17–19], and photoemission measurements [20] necessarily capture both coherent and incoherent parts of the electronic spectrum. Moreover, to cross the metal-to-Mott-insulator transition, angle-resolved photoemission spectroscopy (ARPES) studies need to be carried out as a function of chemical composition as in Ni(S, Se)₂ [21,22], adding the sample quality as another factor to consider. This makes it difficult to separate quasiparticle and background contributions with high

*p.reiss@fkf.mpg.de

resolution and thereby hinders tests of the salient predictions regarding Fermi surface and quasiparticle mass. Recently, however, magnetic quantum oscillations have been observed in the correlated metallic state in high-pressure NiS₂ [14,23]. These experiments track the coherent quasiparticle states up to the Mott transition, revealing that the volume enclosed by the Fermi surface remains essentially unchanged, whereas the carrier mass is strongly renormalized by electronic correlations.

It is of fundamental interest to understand the nature of this high-pressure metallic phase of NiS₂ in more detail, as it forms the basis from which the Mott insulating phase emerges at low pressures. In particular, correctly accounting for any existing magnetic moments at the Ni sites is crucial [24], as such moments will influence the occupation numbers of the Ni *d* orbitals, which are the central ingredient to the Mott physics. For ambient-pressure NiS₂, two successive magnetic phase transitions have been reported, with the transition into the noncollinear antiferromagnetic M1 phase occurring at a temperature $T_{N1} \approx 40$ K, followed by the transition into the weakly ferromagnetic M2 phase below $T_{N2} \approx 30$ K [25,26]. Upon application of hydrostatic pressure or similarly by isoelectronic doping of Ni(S, Se)₂, the M2 phase is suppressed together with the insulating phase [16,24,26] whereas the M1 phase persists into the metallic phase of Ni(S, Se)₂ [24]. Evidence for the existence of the M1 order also in the high-pressure metallic phase of undoped NiS₂ was reported by an electronic transport study which found signatures of a quantum critical point around $p \approx 7.5$ GPa [12,13]. This suggests that the M1 phase persists up to this pressure.

Here, we present a detailed theoretical study of NiS₂ using DFT, which takes the experimentally refined noncollinear magnetic M1 structure into account for the first time [24]. Previous DFT calculations either did not account for magnetic order at all or assumed a collinear alignment of magnetic moments, which, however, breaks the lattice symmetry, in contrast to experimental evidence [19,22,24,27–30]. Our calculations show that the magnetic M1 structure is indeed stable within the high-pressure metallic phase, consistent with previous experimental reports [12,13,24]. In this structure, the magnetic moments reside on the Ni sites and point along the four body diagonals of the cubic unit cell, as shown in Fig. 1. Since DFT cannot explain the Mott insulating transition, our study focuses primarily on the underlying, weakly correlated metallic state which manifests experimentally under high physical (or chemical) pressures, and from which the Mott insulating state emerges below $p_{MIT} \approx 3$ GPa [14]. In particular, our calculations predict a large Fermi surface in the metallic phase, which features a cubical holelike pocket that is robust against changes in pressure p . We also investigate the collapsing metallic phase as a function of Hubbard U and exchange interaction J , and we point out how it differs fundamentally from the experimentally observed Mott insulating phase.

The paper is organized as follows: After briefly presenting the computational methods employed in Sec. II, we describe the changes in the electronic structure between the nonmagnetic phase and the experimentally refined noncollinear magnetic (NCM) phase in Secs. III and IV, respectively, for which DFT predicts metallic ground states. In Sec. V, we

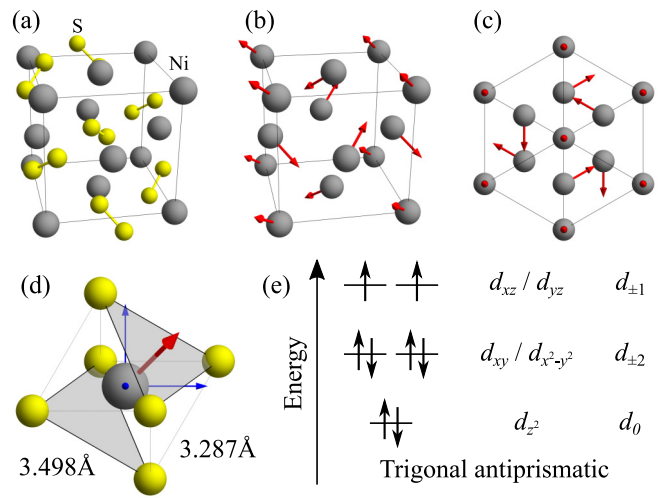


FIG. 1. Crystal and magnetic structure of NiS₂. (a) Crystal structure showing Ni atoms and S dimers. (b) M1 magnetic structure, (c) viewed along (111). The magnetic moments sit on the Ni sites and point along the four body diagonals of the cubic unit cell. For simplicity, the S dimers are omitted in (b) and (c). (d) Local environment of the Ni atoms. The S-S interatomic distances are given. The blue arrows correspond to the axes of the cubic crystallographic unit cell. The noncollinear magnetic moment of the Ni atoms points into the largest S₃ triangle, highlighted by shading. (e) Expected crystal field splitting and orbital occupation of the Ni *d* orbitals in a trigonal antiprismatic coordination of NiS₂. The real and complex labels of the corresponding *d* orbitals are given. The Mott insulating phase occurs due to an individual splitting of the degenerate, half-filled d_{xz} and d_{yz} orbitals, which will form the upper and lower Hubbard bands.

follow the evolution of the metallic, noncollinear magnetic phase under pressure p and compare our results against recent experimental reports. In Sec. VI, we discuss how the metallic phase is suppressed through inclusion of Hubbard interaction U and on-site orbital exchange interaction J , and how the obtained insulating phase differs profoundly from a Mott insulating phase. We then briefly discuss a hypothetical collinear antiferromagnetic phase in Sec. VII; this phase has been discussed in the literature before as an approximation to the noncollinear case [22,29,30]. We end with a brief discussion of the implications of our results in Sec. VIII.

II. METHODS

Band structure calculations were carried out using the WIEN2K and WIENNCM software packages for the nonmagnetic, collinear antiferromagnetic, and noncollinear magnetic calculations, respectively [31–33]. Both packages are based on DFT using linearized augmented plane waves. We used a cutoff $RK_{\max} = 6.0$ (the product of the smallest sphere radius R and the largest plane wave expansion wave vector K_{\max}), for which we found good convergent behavior, and we confirmed that the magnetic moment and Fermi surface volume showed only a negligible dependence up to $RK_{\max} = 8.0$. We employed the Perdew-Burke-Ernzerhof generalized gradient approximation and a high-density mesh of up to 80 000 k points in the full Brillouin zone. The usual energy threshold of -6.0 Ry was used to identify the Ni 1s, 2s, 2p, and 3s

orbitals as core states, as well as the S $1s$, $2s$, and $2p$ orbitals. In WIENNCM, spin-orbit coupling (SOC) is explicitly included, whereas in WIEN2K, SOC is added in a second variational step; however, the effects of SOC are rather weak due to the light atomic cores involved. A Hubbard interaction U and the exchange interaction J were added as tuning parameters for the treatment of the Ni d orbitals using the ORB package. We report the results obtained using the fully localized limit (FLL) correction for double-counting terms (referred to as the self-interaction correction (SIC) in the WIEN2K manual and also sometimes in the literature [34]), and we compare results obtained using the around-mean-field (AMF) method in the Supplemental Material (SM), which show only small deviations that do not affect our conclusions [34–38]. The cubic lattice dimensions under pressure $a(p)$ were taken from experiments [26], and we neglected a reported weak monoclinic distortion in the high-pressure metallic phase, consistent with our own recent measurements [23]. The only internal degree of freedom, i.e., the relative sulfur position x_S/a , was obtained by minimizing the total energy of the nonmagnetic case. We confirmed for ambient pressure, where the noncollinear magnetic moment is the largest, that an energy minimization of the noncollinear case results in essentially the same value for x_S/a . Fermi surfaces were plotted using MATHEMATICA, and extremal Fermi surface cross sections were extracted using Supercell k -Space Extremal Area Finder (SKEAF) [39]. For the plots showing the band structure and the density of states (DOS), we defined zero energy $E = 0$ by the peak of the DOS of the bonding S $3s$ states which are typically found about $E_0 \approx 15$ eV below the Fermi level. The choice of this reference energy provides a stable fixed point for our calculations as it corresponds to electronic states localized between the S dimers, which are the least affected by the magnitude of the magnetic moment on the Ni sites, the Hubbard or exchange interactions of the Ni d states, and the changes in the crystal dimensions under pressure.

III. NONMAGNETIC PHASE

We begin with a description of the predicted electronic structure of NiS₂ in the nonmagnetic phase for $p = 0$ and $U = J = 0$. This case has been covered extensively in the literature before (e.g., Refs. [18,19,22,28–30]). However, it will not only serve as the reference to the noncollinear magnetic phase discussed next, but also motivate a slightly different view of the Ni d suborbitals compared with previous reports. To elucidate the latter point, Fig. 1(a) shows the crystal structure of NiS₂ which promotes the formation of sulfur dimers. These acquire a nominal oxidation state (S₂)²⁻ in the insulating phase and thus leave the Ni atoms in an electronic $3d^8 4s^0$ configuration. In previous reports (e.g., Refs. [27,40–42]), the octahedral coordination of the Ni atoms by S atoms was invoked to explain the separation of Ni t_{2g} and e_g orbitals, with the former fully occupied and the latter half full, which gives the possibility of a Mott transition.

However, the exact nature of the Ni environment as well as the global symmetry of the cubic unit cell indicate that this suggested organization of the Ni d suborbitals is somewhat oversimplified. A closer inspection of the S-S interatomic distances (other than the dimers) shows that they differ by up to

6%, as shown in Fig. 1(d). As a consequence, the Ni site symmetry is actually $\bar{3}$, and the S₆ octahedra are weakly distorted, consisting of S₃ triangles of different sizes [23,26,40]. The key point for this paper is that the largest triangles are found perpendicular to the experimentally refined noncollinear magnetic moments of the central Ni atoms, which point along the unit cell diagonals {111} [cf. Figs. 1(c) and 1(d)]. This establishes the {111} directions as the dominant high-symmetry direction of the Ni environment. This is further evidenced by the observation that the principal axes of the NiS₆ octahedra are not aligned along any high-symmetry directions of the crystal lattice, which may otherwise promote a different high-symmetry direction. As a result, the coordination of Ni is actually trigonal antiprismatic and not octahedral. This induces a crystal field splitting of the Ni d states differently than previously discussed, as shown in Fig. 1(e) [27,40,41]. In the ionic limit, the Ni d_{z^2} , d_{xy} , and $d_{x^2-y^2}$ will be fully occupied, while the degenerate d_{xz} and d_{yz} orbitals will be half filled. Thus, even under the modified Ni d occupation scheme, we obtain an electronic configuration which may lead to the Mott insulating state once electronic correlations are taken into account.

Our DFT calculations are fully consistent with this alternate occupation scheme of the Ni d orbitals. As shown in Fig. 2(a), we recover 12 rather flat, spin-degenerate, and fully occupied bands in the energy window between $E \approx 13$ eV and $E \approx 14$ eV. The orbitally projected density of states demonstrates that these bands have almost exclusive Ni d character, as shown in Figs. 2(b) and 2(c). Towards both lower and higher energies, we find much broader bands with mixed character, dominated by Ni d , S p , and interstitial contributions, which suggests that over this wide energy range, a strong hybridization between Ni and S orbitals occurs. In Fig. 2(d), we integrate the projected DOSs corresponding to the Ni d and S p orbitals over energy. The resulting occupation numbers show that the Ni d and S p orbitals gain almost proportional occupations at low energies $E < 13$ eV, further supporting their spatial overlap. The more the different Ni d suborbitals are aligned towards the S ligands, the larger is their hybridization. Hence the occupation of the Ni d_{xz} and d_{yz} orbitals is the largest at low energies, whereas the Ni d_{z^2} orbital acquires the smallest occupation. This distinct occupation clearly highlights the unique character of the d_{z^2} orbital, which would be incompatible with an assumed octahedral crystal field splitting. Moving towards higher energies across the isolated flat bands, the Coulomb repulsion of the negatively charged S ligands now favors the occupation of the Ni d_{z^2} orbitals which point through the void of the largest S₃ triangles. Consequently, they acquire the largest occupation, followed by the pairwise degenerate Ni d_{xy} and $d_{x^2-y^2}$ and Ni d_{xz} and d_{yz} orbitals. This order of occupation again is consistent with the trigonal antiprismatic crystal field splitting as shown in Fig. 1(e). Moreover, this analysis shows that the crystal field splitting of the Ni d orbitals is roughly a few tenths of an eV and thus smaller than but of similar order to the Hund's coupling, typically assumed to be $J_H \approx 0.7$ eV for Ni (e.g., Ref. [22] and references therein).

Figure 2(d) further shows that at the Fermi level E_F , all Ni d orbitals are almost completely filled within DFT. This is in contrast to the expected half filling of the Ni $3d_{xz}$ and d_{yz}

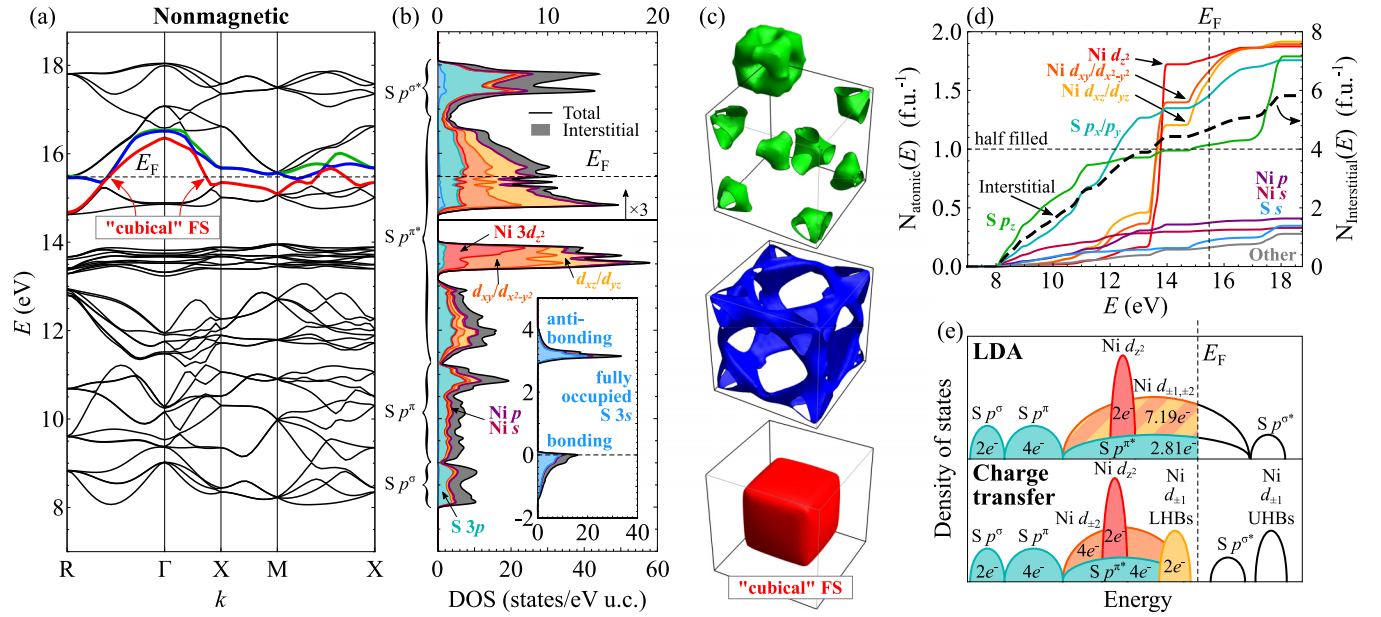


FIG. 2. Calculated electronic structure of NiS_2 in the nonmagnetic phase at ambient pressure. (a) Band structure and (b) density of states (DOS) per unit cell volume (u.c.). The brackets in (b) indicate the extent of the bonding and antibonding $S p^\sigma$ and p^π orbitals; see also (e). The high-symmetry points of the Brillouin zone are defined in Fig. 4(c). In (b), the inset shows the low-energy $S 3s$ states which define the origin of the energy scale employed. Orbital contributions to the DOS are stacked on top of each other. Note that the DOS around the Fermi level E_F was rescaled by a factor 3 for better visibility, as reflected by the upper frame labels. (c) Fermi surface sheets corresponding to the bands crossing the Fermi level [cf. color coding in (a)]. (d) Integrated partial DOSs of the Ni, S, and interstitial states. For the degenerate Ni d and S p states, the contributions are given per individual suborbital. Note that for better visibility, the contributions from the fully occupied $S 3s$ and Ni $3p$ orbitals are not shown, accounting for an additional $10 e^-/\text{f.u.}$ (e) Schematic sketch of the DOS, comparing the computed nonmagnetic structure within the LDA (top) with the expected charge-transfer insulating structure, consistent with DMFT calculations (bottom) [19]. The charge transfer takes place between the almost completely filled Ni $d_{\pm 1} = d_{xz}$ and d_{yz} bands and the partially occupied antibonding $S p^{\pi*}$ band. For the occupation numbers given for the Ni $d_{\pm 1, \pm 2}$ and $S p^{\pi*}$ bands, it was assumed that the interstitial charge is of predominant $S p$ character. LHBs, lower Hubbard bands; UHBs, upper Hubbard bands associated with the Ni $d_{\pm 1}$ bands.

orbitals, which would be the key ingredient for the Mott or charge-transfer insulating phase. Consistently, Figs. 2(b) and 2(e) demonstrate that the states at the Fermi level similarly have mixed character, again mostly Ni d , but with about 20% $S p$ and interstitial contributions, each. As a result, and similar to previous DFT calculations, we interpret the real insulating nature of NiS_2 as a charge-transfer type. We obtain a total valence charge of approximately 15.19 electrons inside each Ni muffin tin, which accounts for the fully occupied Ni $3p$ and the partially occupied Ni $3d$ states. Conversely, there are 6.76 electrons inside the combined muffin tins of the S dimers, including the fully occupied $S 3s$ states and the partially occupied $S 3p$ states. This leaves 6.05 electrons per formula unit associated with the interstitial region, which is likely of predominant $S 3p$ character [43]. As a result, and as shown in Fig. 2(e), a charge transfer of at least $1.19 e^-/\text{f.u.}$ would be required to turn NiS_2 into the experimentally observed insulating phase, depending on the exact character of the interstitial region.

Returning to Fig. 2(a), we find that three bands cross the Fermi level and, hence, the system remains metallic. At ambient pressure, this is a known failure of DFT which makes NiS_2 an interesting system in the first place. Those bands give rise to three Fermi surface sheets, depicted in Fig. 2(c). Since metallized NiS_2 is a compensated system, the enclosed volume of the cubic, holelike Fermi surface sheet is identical

to the combined volume of the other two electronlike sheets. Therefore as a proxy for the charge carrier density, and based on the experimental evidence from ARPES and quantum oscillation studies [14, 21–23], we will focus on the evolution of this cubical Fermi surface sheet throughout this paper.

IV. NONCOLLINEAR MAGNETIC PHASE

As a consequence of the trigonal antiprismatic coordination of the Ni atoms, the observed noncollinear magnetic order in NiS_2 does not break any translation or rotation symmetries [24]. This rather uncommon property is depicted in Fig. 1(c), which shows that the cubic symmetry of the unit cell is retained, and no reconstruction of the Brillouin zone or the Fermi surface is expected. Instead, the effect of the magnetic order is to split the band structure with respect to the nonmagnetic case.

In Fig. 3, we summarize the predicted effects of the noncollinear magnetic structure on the electronic structure at ambient pressure, keeping $U = J = 0$ for now. In order to obtain additional insights into the electronic states, we project the contribution of each state onto spin-up and spin-down character, where the spin orientation is defined locally along the varying magnetic moment inside the atomic spheres [33, 44–48]. In contrast, the interstitial region remains nonmagnetic, and its contributions are assigned to both spin

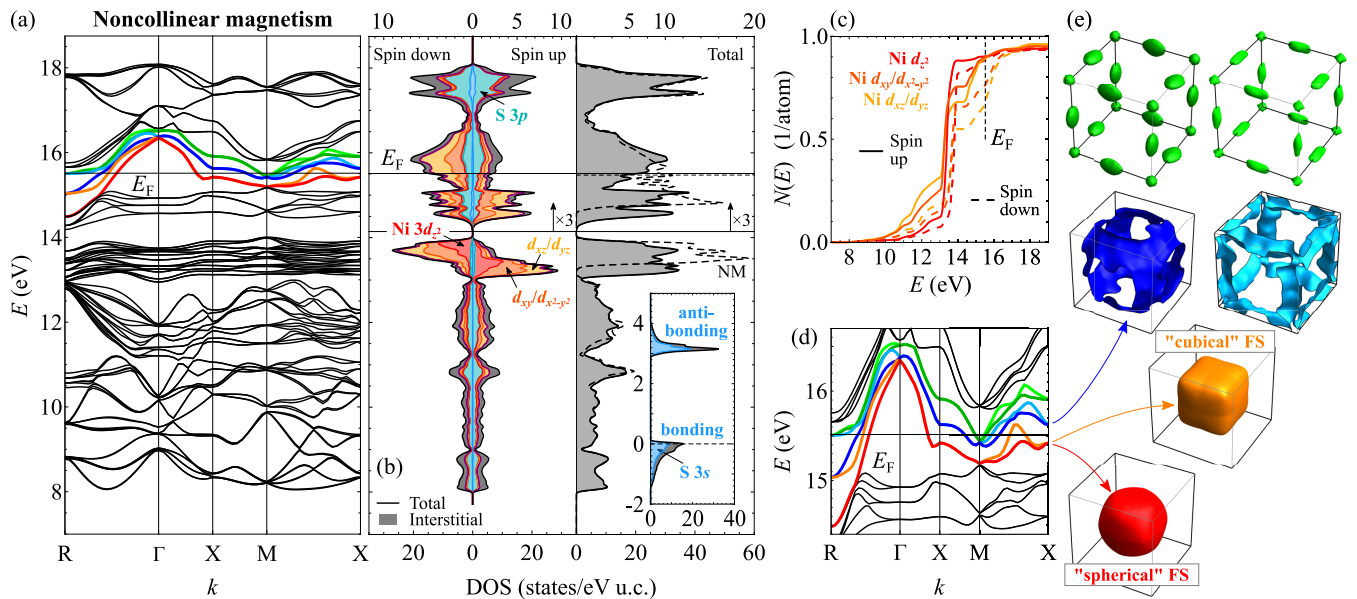


FIG. 3. Calculated electronic structure of NiS_2 in the noncollinear magnetic phase at ambient pressure. (a) Band structure with the bands crossing the Fermi level E_F highlighted in color. The high-symmetry points of the Brillouin zone are defined in Fig. 4(c). (b) Density of states (DOS). On the left, the individual orbital contributions to the spin-projected DOS are stacked on top of each other. On the right, the total DOS is shown, with the total DOS of the nonmagnetic (NM) case included as a dashed curve for reference. Note that the DOS around the Fermi level E_F was rescaled by a factor 3 for better visibility, as reflected by the upper frame labels. For (a) and (b), the energy scale is aligned by the bonding $S\ 3s$ states, as shown in the inset. (c) Orbital occupation as obtained by integrating the projected DOSs for the spin-dependent $\text{Ni}\ d$ orbitals. (d) Zoom into the band structure around the Fermi energy highlighting the k -space-dependent band splitting. (e) Corresponding Fermi surface (FS) sheets using the same color coding as the bands at the Fermi level in (d), as indicated by the arrows.

channels in equal proportions. This analysis reveals that the narrow $\text{Ni}\ d$ states split into two overlapping groups of almost fully spin-polarized bands, as shown in Figs. 3(a) and 3(b). The splitting is about 0.4 eV, which broadens the total DOS peak significantly when compared with the nonmagnetic case. Close to the Fermi level, states with dominant Ni spin-up character are redistributed to lower energies by about 0.3 eV. Again comparing with the nonmagnetic case, this reduces the DOS at the Fermi level to approximately 60% and opens a partial gap right below the Fermi level. This redistribution of the spin-dependent $\text{Ni}\ d$ states gives rise to a net magnetic moment, but it is insufficient to lead to an insulating state as there remains a finite DOS with mixed spin-up and spin-down character at the Fermi level. Correspondingly, our calculations predict a magnetic moment of only $\mu_{\text{Ni}} \approx 0.7\ \mu_B$ for metallic NiS_2 at ambient pressure, compared with the experimental value of approximately $1\ \mu_B$ measured in the Mott insulating state [24].

To trace the origin of the magnetic moment, Fig. 3(c) shows the integrated DOS for the various spin-dependent $\text{Ni}\ d$ orbitals. This shows that all spin-up $\text{Ni}\ d$ orbitals are essentially fully occupied at the Fermi level, as is the spin-down $\text{Ni}\ d_{z^2}$ orbital. The spin-down $\text{Ni}\ d_{xy}$ and $d_{x^2-y^2}$ and $\text{Ni}\ d_{xz}$ and d_{yz} orbitals remain partially occupied, in contrast to the expectations for a Mott or charge-transfer insulator where the $\text{Ni}\ d_{xz}$ and d_{yz} orbitals are expected to be polarized. Inside each Ni muffin tin, we obtain a total valence charge of 15.17 electrons, only marginally less than for the nonmagnetic case. Hence the magnetic moment arises from a spin-dependent reorganization of the $\text{Ni}\ d$ orbital occupations

but does not imply a charge transfer from the Ni atoms to the S dimers or the interstitial region.

Reflecting the spin-dependent changes in the band structure, the Fermi surface also splits. In particular, the cubical Fermi surface sheet predicted for the nonmagnetic phase separates into a smaller nearly spherical pocket and a larger weakly distorted cube, as indicated in Figs. 3(d) and 3(e). The persistence of such a cubical Fermi surface pocket reflects the orientation of the magnetic moments along the crystallographically equivalent $\{111\}$ directions which do not break the cubic lattice symmetry. In contrast, for an assumed collinear antiferromagnetic order, the cubic symmetry would be broken, and a cuboid shape of the Fermi surface would arise, as discussed later in Sec. VII (see also Ref. [29]).

In Fig. 4, we represent this spin-induced splitting of the Fermi surface in more detail. In contrast to collinear ferromagnetic or antiferromagnetic phases, the spin-up and spin-down charge densities of a noncollinear system cannot be treated independently in DFT, but the off-diagonal terms in the spin Hamiltonian must be taken into account fully [33]. Consequently, the predicted Fermi surface does not “spin split” into pure spin-up and spin-down sheets, but rather consists of electronic states with mixed spin contributions. Figure 4 shows this distribution of spin-up and spin-down contributions for the bands associated with the inner spherical and the outer cubical Fermi surface pockets, both of which are holelike. Notably, both bands feature occupied regions in k space where either spin can be dominant. This demonstrates the mixed spin character of the bands and the associated Fermi surface sheets. Comparing the actual Fermi surface sheets (hence states at

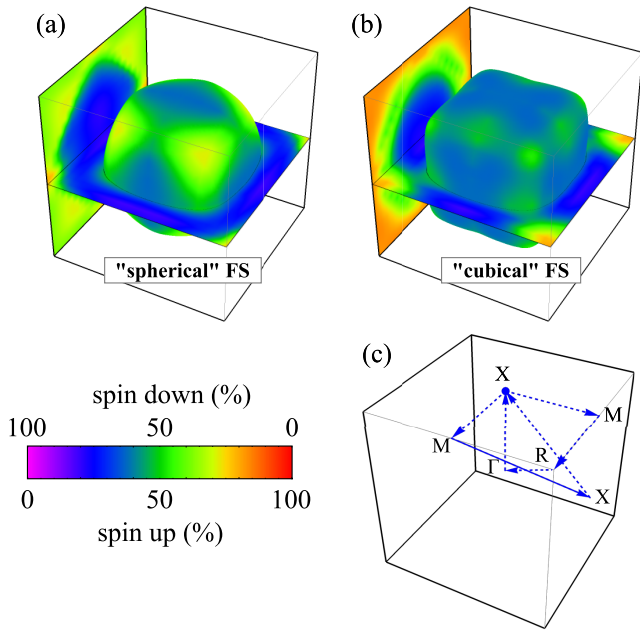


FIG. 4. (a) and (b) Spin projections of the electronic states forming the spherical and cubical Fermi surfaces in the NCM phase for the case $U = J = 0$ and $p = 0$ [see also Fig. 3(e)]. The color coding represents the spin contributions given in relation to the total Ni contribution. The remaining Fermi surface sheets are shown in the SM [38]. (c) Representation of the k path in the first Brillouin zone as used in the band structure plots in Figs. 2, and 3.5.

the Fermi energy), it is noteworthy that the spherical sheet is significantly more mixed than the cube, which is almost exclusively of predominant spin-down character. Moreover, along the reciprocal unit vectors $k_{x,y,z}$ between the Γ and X points [cf. Fig. 4(c) for the definition of the high-symmetry points], the spin configuration of both sheets is identical, whereas along the diagonal vectors $k = (\pm 1, \pm 1, \pm 1)\pi/a$ between the Γ and R points, the spin configuration is maximally different. This k -space-dependent spin splitting can also be seen in the band structure, as shown in Fig. 3(d). Along the path Γ - X the bands do not split, whereas along Γ - R , the splitting is maximal.

V. EFFECT OF HYDROSTATIC PRESSURE

Hydrostatic pressure has been an important experimental tool to investigate NiS_2 , firstly to suppress the Mott insulating phase transition to access the metallic regime around $p_{\text{MIT}} \approx 3$ GPa, and secondly to suppress the magnetic order, with a critical pressure reported to be around 7.5 GPa [12–14,23]. Figures 5(a) and 5(b) show an exemplary band structure and DOS for $p = 8$ GPa, thus close to the suppression of the magnetic phase. Most notably for the Ni d bands, and similarly for the S $3s$ states, the DOS is found to broaden with the peak heights being reduced accordingly, which is a typical effect of hydrostatic pressure. The spin-separated flat Ni d bands move closer together and become less spin polarized, and similarly the DOS around the Fermi level loses some of its spin asymmetry. These trends cause a continuous reduction of the magnetic moment with

increasing pressure, as shown in Fig. 5(d). However, at $p = 8$ GPa, we still obtain a finite moment of $\mu \approx 0.5 \mu_B$ at the Ni sites. Moreover, extrapolating its pressure dependence until the magnetic order is suppressed, our DFT calculations predict a critical pressure $p_c \approx 20$ GPa, much larger than the aforementioned experimental value $p_c \approx 7.5$ GPa [12,13]. This suggests that as in other metallic magnets, the effect of magnetic fluctuations not modeled within DFT plays a crucial role upon approaching the magnetic quantum critical point [50–53].

Despite these clear quantitative changes to the electronic structure, there is no qualitative change in the band structure, and thus we recover the same Fermi surface topology as under ambient pressures, shown in Fig. 5(c). Yet, from the lattice contraction and the increased band width, we expect to observe a small increase in the Fermi surface volume and a reduction of the effective masses. Figures 5(e) and 5(f) confirm these expectations. There, as a measure for sizes of the spherical and cubical Fermi surface pockets and in order to compare these with previous experimental reports [14,23], we extract the predicted quantum oscillation frequencies based on the cross-sectional areas S perpendicular to the applied magnetic field direction $H \parallel a$ (see also Sec. II) [39,49]. Moreover, we estimate the predicted quantum oscillation amplitudes from the curvature factor $(\partial^2 S / \partial k_{\parallel}^2)^{-1/2}$, with k_{\parallel} being the crystal momentum parallel to H [49], and the effective masses from the averaged Fermi velocity along the quantum oscillation orbits. As shown in Figs. 5(c) and 5(e), our calculations within the NCM phase predict a total of three frequencies based on the shape of the cubical and spherical Fermi surface sheets. Such a frequency splitting has indeed been observed for pressures close to the Mott insulating transition where the magnetic M1 phase is expected [14,23]. In contrast, only a single frequency was observed for higher pressures outside the M1 phase, $p > p_c = 7.5$ GPa, in agreement with our predictions for the nonmagnetic Fermi surface topology discussed above. Quantitatively, we find a nearly exact match of the magnitude of the predicted and observed quantum oscillation frequencies, not only as a function of pressure, but also as a function of field angle [23]. This excellent match confirms that our high-pressure calculations correctly reproduce the shape of the Fermi surface as well as the overall charge carrier density. In contrast, our DFT calculations cannot reproduce the experimentally observed effective masses which reach up to $m \approx 7 m_e$ close to the metal-insulator transition [14,23]. In fact, our calculations only yield an effective mass of $m \approx 1 m_e$, as shown in Fig. 5(f). This disparity clearly shows the large degree of electronic correlation at the brink of the Mott insulator transition.

VI. EFFECT OF ON-SITE INTERACTIONS U and J

So far, our treatment of NiS_2 as a nonmagnetic system or as a noncollinear magnet within DFT inevitably led to a metallic ground state, in contrast to the experimental observation of an insulating system at ambient pressures. In order to induce an insulating ground state, we follow the usual approach of considering an on-site Coulomb repulsion on the Ni d orbitals through a Hubbard interaction U . This intra-atomic interaction penalizes doubly occupied orbitals,

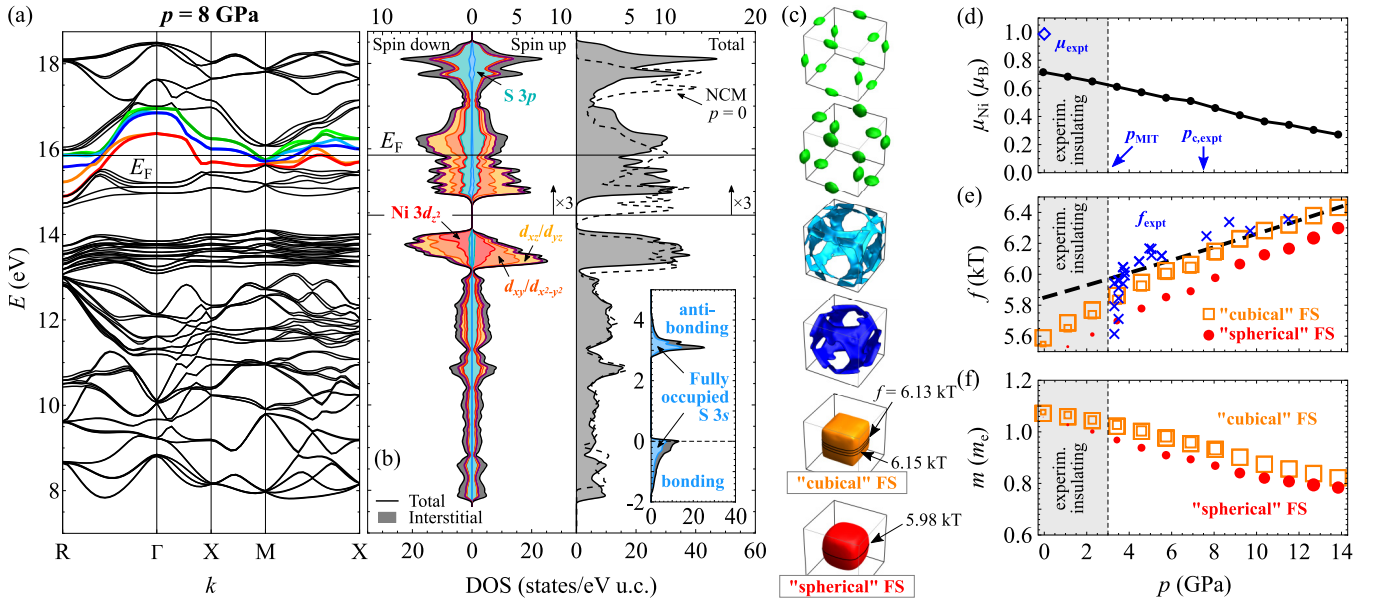


FIG. 5. Predicted electronic structure of NiS₂ in the noncollinear magnetic (NCM) phase under hydrostatic pressures. (a) Band structure and (b) density of states around the Fermi level E_F , and (c) corresponding Fermi surface sheets for a pressure $p \approx 8$ GPa. All predicted quantum oscillation orbits as well as their frequencies are shown for the spherical and cubical Fermi surface sheets. The color coding of the Fermi surface sheets in (c) is identical to the band coloring in (a); see also Figs. 3(d) and 3(e). (d)–(f) Predicted pressure dependence of the magnetic moment, quantum oscillation frequencies of the spherical and cubical Fermi surface sheets, and corresponding effective masses. Experimental data, where available, are shown in blue. Experimental effective masses are significantly larger than the data range shown (up to $m \approx 7 m_e$). In (e) and (f) the symbol sizes for the theoretical values are scaled according to the predicted amplitudes A of quantum oscillations determined from the curvature of the Fermi surface cross section S along the field direction: $A \propto |\partial^2 S / \partial k^2|^{-1/2}$ [49]. μ_{expt} , experimental noncollinear magnetic moment at ambient pressure [24]; p_{MIT} , experimental pressure of the metal-insulator transition in the zero-temperature limit [14]; $p_{c,\text{expt}}$, experimental pressure for antiferromagnetic quantum critical behavior, suggesting the suppression of the M1 magnetic phase [13]; f_{expt} , experimental quantum oscillation frequencies [14,23]; *experim.*, experimental.

which is expected to suppress the Ni-S hybridization and, in combination with the first Hund's rule, should lead to an increasingly spin-polarized electronic configuration. It was argued that both effects combine to eventually induce the Mott or charge-transfer insulating phase. Indeed, previous DFT calculations observed a gap formation at the Fermi level assuming a collinear alignment of magnetic moments [29], as discussed below.

Figures 6(a) and 6(b) show exemplary DOSs for $U = 3$ eV and $U = 6$ eV, using the FLL double-counting correction [35,37]. In the SM, we present the results for the AMF correction, which lead to the exact same conclusions as described below [36,38,54]. The values for U chosen are in the vicinity of the predicted metal-insulator transition, and well into the insulating phase, respectively. They are also similar to experimental values for the Ni d shells [55]. With increasing U , we find that the flat Ni d states shift to significantly lower energy, where they broaden and effectively separate into pure spin-up and spin-down states. Moreover, the spin-up states with dominant Ni d_{xy} and $d_{x^2-y^2}$ and Ni d_{xz} and d_{yz} character split into two distinct peaks, shown around $E = 8$ eV and $E = 10$ eV for $U = 6$ eV in Fig. 6(b). In contrast, the spin-down states and the Ni d_{z^2} states do not show such splitting, but they broaden significantly with increasing U . Close to the Fermi level, the Ni spin-up states are redistributed to lower energies, such that the gap at $E = 14$ eV closes. Conversely, the Ni spin-down states are shifted to higher energies above

the Fermi level. Within DFT + U , it is this spin-dependent separation of electronic states across the Fermi energy that leads to a new gap formation there and thus to the insulating state for $U \gtrsim 3.0$ eV.

Before we discuss the consequences of these energy shifts, we extend our calculations by an on-site exchange interaction J . In contrast to the spin-agnostic Hubbard interaction U , the exchange interaction J favors a ferromagnetic spin alignment on different d suborbitals. Hence it reduces the effective Coulomb repulsion between same-spin charge carriers to $U_{\uparrow\uparrow} = U_{\downarrow\downarrow} = U - J$, whereas the repulsion between opposite-spin charge carriers remains unaffected, $U_{\uparrow\downarrow} = U$ [35,37]. However, recent studies showed mathematically that the best description should be obtained for $J = 0$ in non-collinear cases without spin-orbit coupling [56,57]. For this reason, we will discuss the effect of J only briefly in order to connect to previous collinear DFT studies [22,29] and to account for the possible but weak effects of spin-orbit coupling [58]. Figures 6(b)–6(d) show that the spin-down DOS is almost unaffected by J , whereas in the spin-up DOS, the peak associated with the narrow Ni d_{xy} and $d_{x^2-y^2}$ and Ni d_{z^2} states returns to higher energies. In the limit $J \lesssim U/2$, this leads to a reversal of the order in energy in which the Ni d_{xy} and $d_{x^2-y^2}$ and Ni d_{z^2} orbitals are occupied, compared with the DOS for the case $J = 0$.

Reflecting the changes in the electronic structure as a function of U and J , Fig. 6(e) shows that as the system

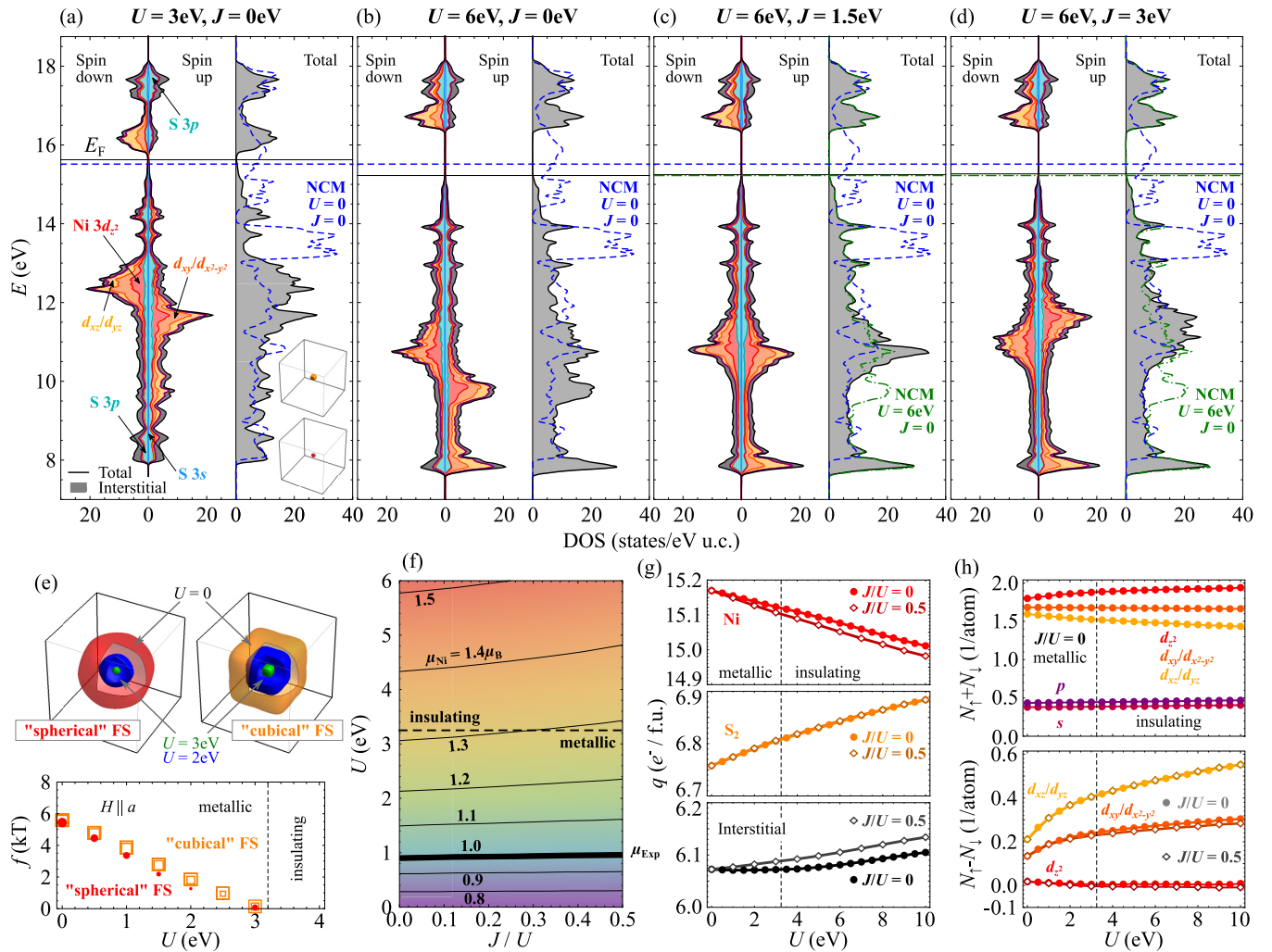


FIG. 6. Evolution of the electronic structure in the NCM phase including on-site Coulomb repulsions using the FLL double-counting correction. (a)–(d) DOS as a function of U and J . The individual atomic and spin contributions to the DOS are stacked on top of each other. For reference, the DOS and Fermi energy for the NCM structure at ambient pressure with $U = J = 0$ are shown as blue dashed curves (see also Fig. 3). Additionally, in (c) and (d), the total DOS and the Fermi energy for the case $J = 0$ [the case shown in (b)] are shown as green dash-dotted curves. (e) Evolution of the predicted Fermi surface with increasing U . Top: Plot of the Fermi surfaces associated with the spherical and cubical sheets. Bottom: Predicted quantum oscillation frequencies for the same sheets, assuming $H \parallel a$. The symbol sizes are scaled as in Fig. 5. The extremal orbits are omitted for clarity. (f) Evolution of the predicted magnetic moment as a function of U and J/U . The experimental value at ambient pressure for insulating NiS_2 is shown as a thick solid black line [24]. The predicted metal-insulator transition is shown as a dashed line. (g) Evolution of the number of valence electrons within the muffin tins of Ni and S atoms, as well as the interstitial regions, as a function of U at fixed J/U . Across the metal-insulator transition, no charge transfer takes place beyond the overall weak trends. (h) Orbital resolved occupation as a function of U for the Ni s , p , and d orbitals, discounting the fully occupied $1s$, $2s$, $2p$, $3s$, and $3p$ orbitals. Top: Total occupation for $J = 0$. Bottom: Spin-differential occupation for fixed J/U .

approaches the insulating phase for increasing U , the predicted Fermi surface shrinks continuously and disappears completely for $U \gtrsim 3.0\text{eV}$. We note that this evolution is essentially independent of the choice of J . As a quantitative measure, Fig. 6(e) also shows how the predicted quantum oscillation frequencies are reduced towards the insulating phase before they disappear at the metal-to-insulator transition. This trend is flat-out contradicted by recent experiments. In particular, our recent quantum oscillation studies revealed that a large Fermi surface of coherent quasiparticles persists right up to the Mott insulating phase transition [14,23]. Similar evidence has been observed in ARPES studies on $\text{Ni}(\text{S}, \text{Se})_2$ [21,22]. Thus a continuously shrinking Fermi surface upon

approaching the insulating phase, as predicted for an increasing U , can be ruled out experimentally.

Further evidence for the shortfall of DFT + U is obtained by considering the evolution of the predicted magnetic moment at the Ni sites. Figure 6(f) shows that with increasing U , the moment grows monotonic as the metallic phase is suppressed and reaches a value of $\mu_{\text{Ni}} \gtrsim 1.3\mu_B$ at the metal-insulator transition, clearly exceeding the ambient-pressure experimental value of approximately $1.0\mu_B$ [24]. The inclusion of the exchange interaction J only reduces the predicted moment slightly. We thus find that both the evolution of the Fermi surface (in the metallic phase) and the magnetic moment are inconsistent with the experimental evidence close

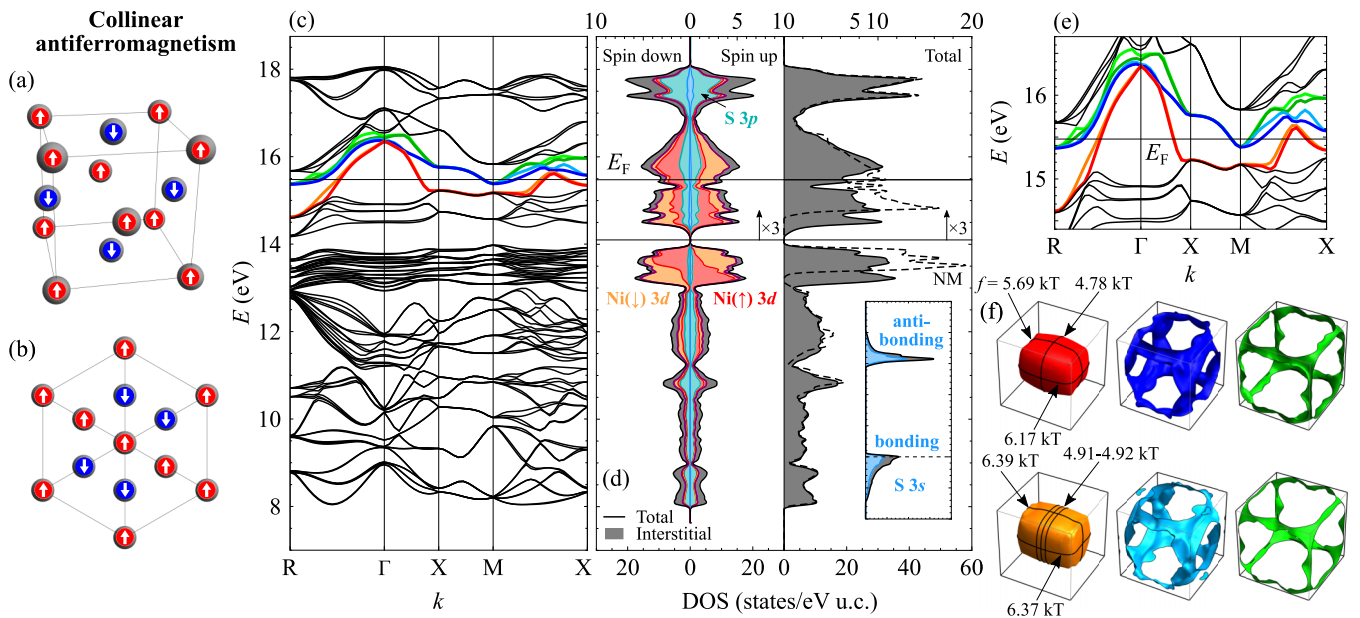


FIG. 7. Assumed but experimentally incorrect collinear magnetic structure of NiS₂. (a) Crystal structure showing the distribution of spin-up and spin-down sites across the unit cell. (b) Same as (a) but viewed along (111). The original threefold, cubic symmetry is broken. For simplicity, the S dimers are omitted in (a) and (b). (c) Band structure and (d) density of states around the Fermi level E_F . The total DOS of the nonmagnetic (NM) case is shown as a dashed curve for reference. (e) Zoom into the band structure in the vicinity of the Fermi level. Note the different band splitting, e.g., at the R point, when compared with the noncollinear case, Fig. 3(d). (f) Predicted Fermi surface sheets. Note that the cubical sheet of the nonmagnetic calculation splits and is deformed into two cuboids. These sheets should therefore give rise to several sets of quantum oscillation frequencies as indicated. Note that the frequencies $f \approx 4.8$ – 4.9 kT were not observed experimentally [14,23]. The color coding of the Fermi surface sheets matches the band colors crossing the Fermi level, as indicated in (c) and (e); see also Figs. 3 and 5.

to the metal-to-insulator transition. Interestingly, we also find that the Fermi surface and the magnetic moment are essentially insensitive to the value of J . This finding reflects that the DOS around the Fermi level remains essentially constant irrespective of J and only the low-energy states are affected; see Figs. 6(b)–6(d).

To understand why DFT + U fails to correctly describe NiS₂ close to the Mott insulator transition, Fig. 6(g) shows the distribution of the valence electrons across the Ni and S atoms and the interstitial region. Across the metal-insulator transition induced by $U \gtrsim 3$ eV, we find that the total charges within the muffin tins of Ni and S do not show any appreciable change. Instead, they evolve smoothly, and fewer than $0.1 e^-$ are transferred from the Ni sites to the S₂ dimers and to the interstitial region up to the phase transition. While this trend goes the right way towards the charge-transfer insulating phase of experimental NiS₂, its prediction within DFT is far too weak. We recover a band insulator, consistent with the predicted shrinking of the Fermi surface. Remarkably, by including an exchange interaction J , the charges around the Ni atoms are slightly reduced, and they bleed into the interstitial region. Evidently, the effect of J is to further delocalize the Ni d states, opposite to the expectations for a Mott or charge-transfer insulator.

As a consequence, the formation of the magnetic moment at the Ni sites must originate from a reorganization of the occupation of the Ni d suborbitals. As shown in Fig. 6(h), we find that with increasing U , the d_{z^2} orbitals become nearly fully occupied, whereas the d_{xz} and d_{yz} orbitals increasingly depopulate. Looking at the spin dependence, Fig. 6(h) also

shows that the d_{xz} and d_{yz} orbitals contribute the most to the magnetic moment, whereas the contribution of the nearly fully occupied d_{z^2} orbitals can be neglected. On the one hand, both trends again agree with the expectations towards the charge-transfer insulator, but the effects within DFT are too weak. On the other hand, in the experimentally insulating phase, a complete occupation of the d_{xy} and $d_{x^2-y^2}$ orbitals would be expected, including a negligible contribution to the magnetic moment. However, our calculations do not indicate any such trend with increasing U , irrespective of J .

VII. COLLINEAR ANTIFERROMAGNETIC PHASE

In order to approximate the noncollinear magnetic phase discussed so far, previous reports studied a hypothetical collinear antiferromagnetic alignment of the Ni magnetic moments, e.g., Ref. [29]. We will now comment on this ordering and how its predictions differ from our noncollinear calculations. As shown in Figs. 7(a) and 7(b), any equal distribution of spin-up and spin-down sites over the unit cell inevitably breaks the cubic threefold symmetry along (111) and hence is incompatible with the experimentally refined cubic crystal structure of NiS₂ [26]. This finding alone indicates that the collinear ordering should be considered as an approximation only. Nevertheless, we compute the resulting electronic structure, for which we obtain a magnetic moment of $\mu_{\text{Ni}} \approx 0.71 \mu_B$, very similar to the size of the noncollinear moment obtained above. Moreover, Figs. 7(c) and 7(d) show the computed band structure and density of states, respectively. To guide the interpretation, we emphasize that

within the collinear antiferromagnetic order (but not within the noncollinear order), all atoms can be assigned to two interpenetrating sublattices with opposite Ni spin orientation. These sublattices can be transformed into one another, e.g., by a reflection on the xy plane, followed by a translation by $(0.5, 0, 0.5)$ and a subsequent spin flip. Consequently, in the absence of spin-orbit coupling, the spin-up and spin-down densities within DFT are identical subject to the above symmetry operation and hence produce the same density of states, albeit with opposite spin contributions. Adding a weak spin-orbit coupling as in NiS_2 , a small energy splitting of the spin-up and spin-down states occurs. We recover these expectations in Figs. 7(c) and 7(d) quite clearly: On the one hand, the total spin-dependent densities of states are effectively identical and the atomic contributions are indeed inverted by the spin. This finding is in stark contrast to the results of the noncollinear order, where the spin-up and spin-down density of states are clearly different; cf. Fig. 3(b). On the other hand, all bands within the collinear antiferromagnetic order are weakly split in energy. While the magnitude of this splitting is similar to that in the noncollinear magnetic case discussed above, there are qualitative differences. For example, within the collinear ordering, the lowest two bands crossing the Fermi level are degenerate at the R point in the Brillouin zone [red and orange bands in Fig. 7(e)], but they fully split in the noncollinear case [see Fig. 3(d)].

Accounting for the weak spin-orbit induced band splitting within the collinear antiferromagnetic order, the predicted Fermi surface sheets split in comparison to the nonmagnetic calculation, as shown in Figs. 7(f) and 2(c). Moreover, reflecting the loss of the cubic symmetry, the formerly cubical Fermi surface sheet deforms into two rather similar cuboids, shown in red and orange in Fig. 7(f). In order to compare the predictions of such Fermi surface sheets against experimental evidence, we first emphasize that the broken cubic symmetry will lead to domain formation in a real crystal. Therefore any quantum oscillation measurement will pick up frequencies originating from domains with different orientations, which translates to different field orientations in our theoretical study. In particular, for a field applied nominally along (100), we need to consider the additional orientations (010) and (001). As indicated in Fig. 7(f), the cuboid deformation of the Fermi surface sheets gives rise to several different extremal orbits which translate to the given quantum oscillation frequencies. While a frequency of $f \approx 5.7$ kT is similar to the ambient-pressure predictions for the noncollinear case [Fig. 5(e)] and thus would likely match our high-pressure experimental observations [14,23], the frequencies $f \approx 6.2$ – 6.4 kT are significantly larger and hence would clearly exceed the observed frequencies under pressure. The discrepancy is even more severe for the lower frequencies in the range $f \approx 4.8$ – 4.9 kT as no similar frequencies could be observed experimentally at all. While one should be careful when drawing conclusions from the nonobservation of specific quantum oscillation frequencies, we note that the frequencies $f \approx 4.8$ – 4.9 kT and $f \approx 6.2$ – 6.4 kT originate from the same Fermi surface sheet as the clearly observable frequencies around $f \approx 5.7$ kT [14,23]. As such, they should share similar scattering rates and curvature factors, while the effective masses for the lower frequencies $f \approx 4.8$ – 4.9 kT are

expected to be about 40% smaller due to the smaller Fermi surface cross section (equivalent to a larger Fermi velocity). As such, these lower frequencies should in fact be easier to observe than the $f \approx 5.7$ kT frequencies, in clear contrast to the experimental evidence. Finally, the angular dependence of the observable quantum oscillation frequencies is in excellent agreement with a nearly cubical Fermi surface sheet [23], which further demonstrates the incompatibility of the cuboid shape. In conclusion, from our calculations, we identified multiple observables which rule out the formation of a collinear antiferromagnetic order in NiS_2 in the high-pressure metallic phase.

VIII. DISCUSSION

Having mapped out the dependence of the electronic structure of magnetic NiS_2 as a function of magnetic ordering, hydrostatic pressure p , and electronic interactions U and J , we now comment on the implications of our results. First of all, we reiterate that for ambient pressure, and in the absence of a Hubbard U , our calculations wrongly predict a metallic ground state irrespective of the assumed magnetic order, which is the expected shortcoming of DFT. Nevertheless, our results assuming the experimentally refined noncollinear magnetic order successfully describe key aspects of the experimentally accessible metallic phase under high pressures. They lay out the weakly correlated electronic structure from which the Mott insulating phase emerges at lower pressures.

Specifically, our high-pressure calculations demonstrate that it is essential to account for the experimentally refined noncollinear magnetic order in NiS_2 to describe the observed Fermi surface in the metallic phase. Our predicted quantum oscillation frequencies match the experimentally observed ones almost perfectly, in magnitude, field angle, pressure dependence, and the frequency splitting within the magnetic phase, as demonstrated in Fig. 5(e) and discussed in Refs. [14,23]. In contrast, a nonmagnetic phase cannot explain the observed frequency splitting, whereas a collinear magnetic structure would predict further quantum oscillation frequencies which were not observed experimentally [14,21–23].

Regarding the insulating phase, we note that our DFT calculations cannot predict the nature of the insulating ground state correctly, even when extended by an intra-atomic Hubbard repulsion U or an exchange interaction J . Moreover, DFT + U (+ J) calculations also do not represent the correlated metallic state near the Mott transition correctly: While an insulating state emerges for $U \gtrsim 3.0$ eV, the continuously shrinking and eventually disappearing Fermi surface contrasts with experimental evidence on approaching the metal-to-insulator transition from the metallic side [14,21–23]. Moreover, the occupation numbers of the Ni d and S p orbitals do not match the expectations for a Mott or charge-transfer insulator, but those for a band insulator, even deep inside the insulating phase for large values of U . Both findings provide strong support for a mechanism driven by enhanced electronic correlations and a vanishing quasiparticle residue instead, in agreement with the Brinkman-Rice scenario [3]. Nevertheless, a finite U captures some trends correctly, such as a small charge transfer from Ni to S sites and a gradual

suppression of the DOS peak of the Ni d states at $E \approx 13\text{--}14$ eV, on top of the peak height suppression attributed to the noncollinear magnetic order (see also Fig. 3). Such a suppression was observed in photoemission studies, where it was attributed to a coherent-to-incoherent crossover [21]. In contrast, our results show that a similar effect may even occur for coherent electronic states.

In contrast to the Hubbard U term, the exchange interaction J does not provide support for the insulating state. While it strongly affects the DOS away from the Fermi energy, it leaves the DOS around the Fermi energy essentially unaffected. The influence of J is thus complementary to U , and the often encountered simplification to perform calculations with an effective $U_{\text{eff}} = U - J$ does not apply here [31,59,60]. Moreover, a finite J appears to weakly delocalize the Ni d states, in contrast to the expectations within the insulating phase. We therefore suggest keeping $J = 0$ for future calculations, in excellent agreement with recent theoretical considerations [56,57].

Our calculations also show that the predicted ambient-pressure magnetic moment μ_{Ni} for any finite U in the insulating phase overestimates the experimental value by at least 30%, as shown in Fig. 6(f). This mismatch likely is the result of the incorrect occupation of the Ni d orbitals as discussed above. However, in the high-pressure metallic phase, where the orbital occupation is likely correct as evidenced by the correct Fermi surface topology, the critical pressure p_c at which magnetism is suppressed is overestimated by a factor ≈ 3 [Fig. 5(d)]. This overestimate may be interpreted as an indicator for strong spin fluctuations. Spin fluctuations are known to significantly reduce the ordered magnetic moments, critical temperatures, and critical pressures [50–53]. Indeed, experimental evidence for the importance of spin fluctuations has previously been identified in NiS₂ due to significant non-Fermi-liquid transport behavior

across the magnetic quantum phase transition [12,13]. Here, using DFT, the magnetic moments are treated only on a mean-field level, and thus overestimated moments in the metallic phase are to be expected.

In conclusion, our DFT calculations of metallized NiS₂ significantly extend previous studies which either ignored magnetic order altogether or assumed a collinear antiferromagnetic order. By incorporating the noncollinear magnetic order from the outset, our calculations correctly describe the Fermi surface observed in high-pressure quantum oscillation measurements. We find that adding in intra-atomic Hubbard and exchange interactions at the DFT level induces an insulating state but misses key aspects of the correlated metallic state on the threshold of Mott localization, namely, the robust Fermi surface volume and the magnitude of the quasiparticle mass renormalization. Further experimental and theoretical studies, including DMFT, will be required to achieve a quantitative description of the correlated metal on approaching the Mott insulating transition and in the vicinity of the pressure-induced magnetic quantum critical point.

The data that support the findings of this study are available through the Edmond open access data archive at the Max Planck Digital Library [61].

ACKNOWLEDGMENTS

We thank Konstantin Semeniuk and Hui Chang for insightful discussions. P.R. acknowledges support from the Oxford Quantum Materials Platform Grant (EPSRC Grant No. EP/M020517/1). S.F. and F.M.G. acknowledge support from EPSRC Grants No. EP/N026691/1 and No. EP/K012894/1. S.F. acknowledges support by the ERC and the Alexander von Humboldt Foundation under Grants No. 271982 EICMSC and No. 3.3-DEU/1134964 FL, respectively.

-
- [1] M. Imada, A. Fujimori, and Y. Tokura, Metal-insulator transitions, *Rev. Mod. Phys.* **70**, 1039 (1998).
 - [2] J. H. de Boer and E. J. W. Verwey, Semi-conductors with partially and with completely filled $3d$ -lattice bands, *Proc. Phys. Soc.* **49**, 59 (1937).
 - [3] W. F. Brinkman and T. M. Rice, Application of Gutzwiller's variational method to the metal-insulator transition, *Phys. Rev. B* **2**, 4302 (1970).
 - [4] A. Georges, G. Kotliar, W. Krauth, and M. J. Rozenberg, Dynamical mean-field theory of strongly correlated fermion systems and the limit of infinite dimensions, *Rev. Mod. Phys.* **68**, 13 (1996).
 - [5] Y. Kohsaka, T. Hanaguri, M. Azuma, M. Takano, J. C. Davis, and H. Takagi, Visualization of the emergence of the pseudogap state and the evolution to superconductivity in a lightly hole-doped Mott insulator, *Nat. Phys.* **8**, 534 (2012).
 - [6] S. Lefebvre, P. Wzietek, S. Brown, C. Bourbonnais, D. Jérôme, C. Mézière, M. Fourmigué, and P. Batail, Mott Transition, Antiferromagnetism, and Unconventional Superconductivity in Layered Organic Superconductors, *Phys. Rev. Lett.* **85**, 5420 (2000).
 - [7] L. de' Medici, G. Giovannetti, and M. Capone, Selective Mott Physics as a Key to Iron Superconductors, *Phys. Rev. Lett.* **112**, 177001 (2014).
 - [8] F. J. Morin, Oxides Which Show a Metal-to-Insulator Transition at the Neel Temperature, *Phys. Rev. Lett.* **3**, 34 (1959).
 - [9] D. B. McWhan, A. Menth, J. P. Remeika, W. F. Brinkman, and T. M. Rice, Metal-insulator transitions in pure and doped V₂O₃, *Phys. Rev. B* **7**, 1920 (1973).
 - [10] S. A. Carter, T. F. Rosenbaum, M. Lu, H. M. Jaeger, P. Metcalf, J. M. Honig, and J. Spalek, Magnetic and transport studies of pure V₂O₃ under pressure, *Phys. Rev. B* **49**, 7898 (1994).
 - [11] A. G. Gavriliuk, I. A. Trojan, and V. V. Struzhkin, Insulator-Metal Transition in Highly Compressed NiO, *Phys. Rev. Lett.* **109**, 086402 (2012).
 - [12] N. Takeshita, S. Takashima, C. Terakura, H. Nishikubo, S. Miyasaka, M. Nohara, Y. Tokura, and H. Takagi, Quantum criticality and disorder in the antiferromagnetic critical point of NiS₂ pyrite, [arXiv:0704.0591](https://arxiv.org/abs/0704.0591).

- [13] P. G. Niklowitz, P. L. Alireza, M. J. Steiner, G. G. Lonzarich, D. Braithwaite, G. Knebel, J. Flouquet, and J. A. Wilson, Unconventional resistivity at the border of metallic antiferromagnetism in NiS₂, *Phys. Rev. B* **77**, 115135 (2008).
- [14] S. Friedemann, H. Chang, M. B. Gamza, P. Reiss, X. Chen, P. L. Alireza, W. A. Coniglio, D. E. Graf, S. Tozer, and F. M. Grosche, Large Fermi surface of heavy electrons at the border of Mott insulating state in NiS₂, *Sci. Rep.* **6**, 25335 (2016).
- [15] X. Yao, Y.-K. Kuo, D. K. Powell, J. W. Brill, and J. M. Honig, Magnetic susceptibility and heat-capacity studies of NiS_{2-x}Se_x single crystals: A study of transitions at nonzero temperature, *Phys. Rev. B* **56**, 7129 (1997).
- [16] M. Matsuura, H. Hiraka, K. Yamada, and Y. Endoh, Magnetic phase diagram and metal-insulator transition of NiS_{2-x}Se_x, *J. Phys. Soc. Jpn.* **69**, 1503 (2000).
- [17] K. Sato, Reflectivity spectra and optical constants of pyrites (FeS₂, CoS₂ and NiS₂) between 0.2 and 4.4 eV, *J. Phys. Soc. Jpn.* **53**, 1617 (1984).
- [18] A. Perucchi, C. Marini, M. Valentini, P. Postorino, R. Sopracase, P. Dore, P. Hansmann, O. Jepsen, G. Sangiovanni, A. Toschi, K. Held, D. Topwal, D. D. Sarma, and S. Lupi, Pressure and alloying effects on the metal to insulator transition in NiS_{2-x}Se_x studied by infrared spectroscopy, *Phys. Rev. B* **80**, 073101 (2009).
- [19] J. Kuneš, L. Baldassarre, B. Schächner, K. Rabia, C. A. Kuntscher, D. M. Korotin, V. I. Anisimov, J. A. McLeod, E. Z. Kurmaev, and A. Moewes, Metal-insulator transition in NiS_{2-x}Se_x, *Phys. Rev. B* **81**, 035122 (2010).
- [20] H. Ishii, K. Kanai, Y. Tezuka, S. Shin, S. Miyasaka, and H. Takagi, Resonant inverse photoemission study of NiS_{2-x}Se_x, *J. Electron Spectrosc. Relat. Phenom.* **92**, 77 (1998).
- [21] H. C. Xu, Y. Zhang, M. Xu, R. Peng, X. P. Shen, V. N. Strocov, M. Shi, M. Kobayashi, T. Schmitt, B. P. Xie, and D. L. Feng, Direct Observation of the Bandwidth Control Mott Transition in the NiS_{2-x}Se_x Multiband System, *Phys. Rev. Lett.* **112**, 087603 (2014).
- [22] B. G. Jang, G. Han, I. Park, D. Kim, Y. Y. Koh, Y. Kim, W. Kyung, H.-D. Kim, C.-M. Cheng, K.-D. Tsuei, K. D. Lee, N. Hur, J. H. Shim, C. Kim, and G. Kotliar, Direct observation of kink evolution due to Hund's coupling on approach to metal-insulator transition in NiS_{2-x}Se_x, *Nat. Commun.* **12**, 1208 (2021).
- [23] K. Semeniuk, H. Chang, J. Baglo, S. Friedemann, A. Grockowiak, W. A. Coniglio, M. B. Gamza, P. Reiss, P. Alireza, I. Leermakers, A. McCollam, S. Tozer, and F. M. Grosche, Truncated mass divergence in a Mott metal, [arXiv:2202.04024](https://arxiv.org/abs/2202.04024).
- [24] S. Yano, D. Louca, J. Yang, U. Chatterjee, D. E. Bugaris, D. Y. Chung, L. Peng, M. Grayson, and M. G. Kanatzidis, Magnetic structure of NiS_{2-x}Se_x, *Phys. Rev. B* **93**, 024409 (2016).
- [25] M. Matsuura, Y. Endoh, H. Hiraka, K. Yamada, A. S. Mishchenko, N. Nagaosa, and I. V. Solovyev, Classical and quantum spin dynamics in the fcc antiferromagnet NiS₂ with frustration, *Phys. Rev. B* **68**, 094409 (2003).
- [26] Y. Feng, R. Jaramillo, A. Banerjee, J. M. Honig, and T. F. Rosenbaum, Magnetism, structure, and charge correlation at a pressure-induced Mott-Hubbard insulator-metal transition, *Phys. Rev. B* **83**, 035106 (2011).
- [27] D. W. Bullett, Electronic structure of 3d pyrite- and marcasite-type sulphides, *J. Phys. C: Solid State Phys.* **15**, 6163 (1982).
- [28] J.-H. Wang, Z. Cheng, J.-L. Brédas, and M. Liu, Electronic and vibrational properties of nickel sulfides from first principles, *J. Chem. Phys.* **127**, 214705 (2007).
- [29] C. Schuster, M. Gatti, and A. Rubio, Electronic and magnetic properties of NiS₂, NiSe and NiSe₂ by a combination of theoretical methods, *Eur. Phys. J. B* **85**, 325 (2012).
- [30] E. Day-Roberts, R. M. Fernandes, and T. Birol, Gating-induced Mott transition in NiS₂, [arXiv:2203.13355](https://arxiv.org/abs/2203.13355).
- [31] K. Schwarz and P. Blaha, Solid state calculations using WIEN2k, *Comput. Mater. Sci.* **28**, 259 (2003).
- [32] P. Blaha, K. Schwarz, F. Tran, R. Laskowski, G. K. H. Madsen, and L. D. Marks, WIEN2k: An APW+lo program for calculating the properties of solids, *J. Chem. Phys.* **152**, 074101 (2020).
- [33] R. Laskowski, G. K. H. Madsen, P. Blaha, and K. Schwarz, Magnetic structure and electric-field gradients of uranium dioxide: An *ab initio* study, *Phys. Rev. B* **69**, 140408(R) (2004).
- [34] P. Novák, F. Boucher, P. Gressier, P. Blaha, and K. Schwarz, Electronic structure of the mixed valence system (YM)₂BaNiO₅ (M = Ca, Sr), *Phys. Rev. B* **63**, 235114 (2001).
- [35] V. I. Anisimov, I. V. Solovyev, M. A. Korotin, M. T. Czyżyk, and G. A. Sawatzky, Density-functional theory and NiO photoemission spectra, *Phys. Rev. B* **48**, 16929 (1993).
- [36] M. T. Czyżyk and G. A. Sawatzky, Local-density functional and on-site correlations: The electronic structure of La₂CuO₄ and LaCuO₃, *Phys. Rev. B* **49**, 14211 (1994).
- [37] A. I. Liechtenstein, V. I. Anisimov, and J. Zaanen, Density-functional theory and strong interactions: Orbital ordering in Mott-Hubbard insulators, *Phys. Rev. B* **52**, R5467 (1995).
- [38] See Supplemental Material at <http://link.aps.org/supplemental/10.1103/PhysRevB.106.205131> for further details regarding the noncollinear order, as well as further calculations supporting the main conclusions of this paper.
- [39] P. M. C. Rourke and S. R. Julian, Numerical extraction of de Haas-van Alphen frequencies from calculated band energies, *Comput. Phys. Commun.* **183**, 324 (2012).
- [40] E. Nowack, D. Schwarzenbach, and T. Hahn, Charge densities in CoS₂ and NiS₂ (pyrite structure), *Acta Crystallogr., Sect. B: Struct. Sci.* **47**, 650 (1991).
- [41] J. M. Honig and J. Spalek, Electronic properties of NiS_{2-x}Se_x single crystals: From magnetic Mott-Hubbard insulators to normal metals, *Chem. Mater.* **10**, 2910 (1998).
- [42] A. Fujimori, K. Mamiya, T. Mizokawa, T. Miyadai, T. Sekiguchi, H. Takahashi, N. Mōri, and S. Suga, Resonant photoemission study of pyrite-type NiS₂, CoS₂ and FeS₂, *Phys. Rev. B* **54**, 16329 (1996).
- [43] The number 6.05 also includes contributions from the low-energy S 3s orbitals leaking out of the S muffin tins which were not integrated in Fig. 2(d).
- [44] J. Kubler, K. H. Hock, J. Sticht, and A. R. Williams, Density functional theory of non-collinear magnetism, *J. Phys. F: Met. Phys.* **18**, 469 (1988).
- [45] L. Nordström and D. J. Singh, Noncollinear Intra-atomic Magnetism, *Phys. Rev. Lett.* **76**, 4420 (1996).
- [46] K. Knöpfle, L. Sandratskii, and J. Kübler, Noncollinear magnetic order in U₃Bi₄, *J. Alloys Compd.* **309**, 31 (2000).
- [47] P. Kurz, G. Bihlmayer, S. Blügel, K. Hirai, and T. Asada, Comment on "Ultrathin Mn films on Cu(111) substrates: Frustrated antiferromagnetic order", *Phys. Rev. B* **63**, 096401 (2001).
- [48] P. Kurz, F. Förster, L. Nordström, G. Bihlmayer, and S. Blügel, *Ab initio* treatment of noncollinear magnets with the full-

- potential linearized augmented plane wave method, *Phys. Rev. B* **69**, 024415 (2004).
- [49] D. Shoenberg, *Magnetic Oscillations in Metals* (Cambridge University Press, Cambridge, 1984).
- [50] T. Moriya and A. Kawabata, Effect of spin fluctuations on itinerant electron ferromagnetism, *J. Phys. Soc. Jpn.* **34**, 639 (1973).
- [51] G. G. Lonzarich and L. Taillefer, Effect of spin fluctuations on the magnetic equation of state of ferromagnetic or nearly ferromagnetic metals, *J. Phys. C: Solid State Phys.* **18**, 4339 (1985).
- [52] T. Moriya, *Spin Fluctuations in Itinerant Electron Magnetism*, Springer Series in Solid-State Sciences Vol. 56 (Springer-Verlag, Berlin, 1985).
- [53] M. Brando, D. Belitz, F. M. Grosche, and T. R. Kirkpatrick, Metallic quantum ferromagnets, *Rev. Mod. Phys.* **88**, 025006 (2016).
- [54] E. R. Ylvisaker, W. E. Pickett, and K. Koepf, Anisotropy and magnetism in the LSDA+ U method, *Phys. Rev. B* **79**, 035103 (2009).
- [55] E. Antonides, E. C. Janse, and G. A. Sawatzky, LMM Auger spectra of Cu, Zn, Ga, and Ge. I. Transition probabilities, term splittings, and effective Coulomb interaction, *Phys. Rev. B* **15**, 1669 (1977).
- [56] M. E. A. Coury, S. L. Dudarev, W. M. C. Foulkes, A. P. Horsfield, P.-W. Ma, and J. S. Spencer, Hubbard-like Hamiltonians for interacting electrons in s , p , and d orbitals, *Phys. Rev. B* **93**, 075101 (2016).
- [57] S. L. Dudarev, P. Liu, D. A. Andersson, C. R. Stanek, T. Ozaki, and C. Franchini, Parametrization of LSDA+ U for noncollinear magnetic configurations: Multipolar magnetism in UO_2 , *Phys. Rev. Mater.* **3**, 083802 (2019).
- [58] M. Charlebois, J.-B. Morée, K. Nakamura, Y. Nomura, T. Tadano, Y. Yoshimoto, Y. Yamaji, T. Hasegawa, K. Matsuhira, and M. Imada, *Ab initio* derivation of low-energy Hamiltonians for systems with strong spin-orbit interaction: Application to $\text{Ca}_5\text{Ir}_3\text{O}_{12}$, *Phys. Rev. B* **104**, 075153 (2021).
- [59] S. L. Dudarev, G. A. Botton, S. Y. Savrasov, C. J. Humphreys, and A. P. Sutton, Electron-energy-loss spectra and the structural stability of nickel oxide: An LSDA+ U study, *Phys. Rev. B* **57**, 1505 (1998).
- [60] M. Cococcioni and S. de Gironcoli, Linear response approach to the calculation of the effective interaction parameters in the LDA + U method, *Phys. Rev. B* **71**, 035105 (2005).
- [61] P. Reiss, S. Friedemann, and F. M. Grosche, *Ab initio* electronic structure of metallized NiS_2 in the noncollinear magnetic phase (2022), <https://doi.org/10.17617/3.MOYBSY>.